Wiley Analytical Science

Specific Heat Capacity Determination by DSC

April 19, 10:00am - 11:00am EDT

Specific heat capacity (cp) is an important, temperature-dependent material property and is often specified in material data sheets. It is a key property for improving technical processes such as injection molding, spray drying, or crystallization, as well as for the safety analysis of chemical processes and the design of chemical reactors.

Watch this session during the WAS Virtual Conference:

Dr. Jürgen Schawe

Register Now

This talk is sponsored by METTLER TOLEDO

ADVANCED OPTICAL MATERIALS
www.advopticalmat.de

Tuning the Bandgaps of $(Al_xGa_{1-x})_2O_3$ Alloyed Thin Films for High-Performance Solar-Blind Ultraviolet Fully Covered Photodetectors

Xiangyu Xu, Ziqian Sheng, Jueli Shi, Xin Chen, Yaxin He, Wenjing Xu, Xu Zhang, Duanyang Chen, Hongji Qi, and Kelvin H. L. Zhang**

Ga_2O_3 is a promising semiconductor for deep ultraviolet optoelectronics, because of its ultrawide bandgap of 4.85 eV. Here, the bandgap modulation of $(Al_xGa_{1-x})_2O_3$ thin films through varying Al contents is reported –and the achievement of high-performance photodetectors sensitive to the entire solar-blind UV bands. It is shown that the bandgaps of $(Al_xGa_{1-x})_2O_3$ can be widely tuned from 4.85 eV to 5.9 eV. Solar-blind ultraviolet photodetectors based on the $(Al_xGa_{1-x})_2O_3$ films show detection cut-off wavelengths varying from 263 to 236 nm, and response peaks varying from 238 to 209 nm. The photodetectors exhibit high performance with a high specific detectivity (up to 10^{15} Jones), low dark current (<0.35 nA), large photodark current ratio (≈10^7), UV–vis rejection ratio (>10^5), and long-term device stability. Furthermore, a combination of high-resolution X-ray photoemission spectroscopy and density functional theory calculations is used to reveal insights into the evolution of electronic structures of $(Al_xGa_{1-x})_2O_3$. The wide variations of the bandgap of $(Al_xGa_{1-x})_2O_3$ mainly result from the upshift of the conduction band edges induced by the high energy Al 3s state hybridizing with the Ga 4s-derived conduction band, while the valence band edge keeps almost the same for different Al content.

1. Introduction

Earth's atmosphere is known to intercept deep ultraviolet light below 280 nm. Oxygen strongly absorbs vacuum ultraviolet light (10–200 nm), only detectable in vacuum.[1–4] Ultraviolet light (200–280 nm) is nearly undetectable on Earth's surface due to the ozone layer's strong absorption in the stratosphere, known as solar-blind ultraviolet light. The detection of this band has the characteristics of low interference and low false alarm. Solar-blind ultraviolet photodetectors have wide-ranging applications including flame detection, ozone hole monitor, power grid safety monitoring, missile tracking, and biochemical analysis.[5–8] Beta phase gallium oxide (β-Ga_2O_3) emerges as the most promising semiconductor material for next generation solar-blind ultraviolet photodetectors, because of its ultrawide bandgap of 4.85 eV, which makes the material selectively sensitive to solar-blind UV wavelength.[9–12] Such inherit merits outperform conventional wide bandgap semiconductors such as SiC and GaN, whose intrinsic bandgaps are not large enough for direct solar-blind UV detection.[13] Compared to other emerging ultrawide bandgap low-dimensional materials such as $FePSe_3$ and BiOCl,[14,15] Ga_2O_3 based semiconductors have the advantage of ease to achieving large-scale thin films and devices.

Al_2O_3 has an even larger bandgap of 8.8 eV.[16] Alloying Ga_2O_3 with Al_2O_3 to form $(Al_xGa_{1-x})_2O_3$ ternary semiconductor offers an opportunity to widely tune the bandgaps from 4.85 to 8.8 eV.[13,17,18] **Figure 1**a shows the schematic energy band diagram for Ga_2O_3 and Al_2O_3. Both the valence bands (VBs) of Ga_2O_3 and Al_2O_3 are dominated by filled O $2p^6$ states, while the conduction bands (CBs) are mainly formed by empty Ga 4s or Al 3s orbitals. It can be envisioned that alloying Al_2O_3

X. Xu, Z. Sheng, J. Shi, X. Chen, Y. He, W. Xu, X. Zhang, K. H. L. Zhang
State Key Laboratory of Physical Chemistry of Solid Surfaces
College of Chemistry and Chemical Engineering
Xiamen University
Xiamen 361005, P. R. China
E-mail: kelvinzhang@xmu.edu.cn
X. Xu, Z. Sheng, K. H. L. Zhang
Shenzhen Research Institute of Xiamen University
Shenzhen 518000, P. R. China

D. Chen, H. Qi
Key Laboratory of Materials for High Power Laser
Shanghai Institute of Optics and Fine Mechanics
Chinese Academy of Sciences
Shanghai 201800, P. R. China
E-mail: chenduanyang@siom.ac.cn
D. Chen, H. Qi
Research Center of Laser Crystal
Shanghai Institute of Optics and Fine Mechanics
Chinese Academy of Sciences
Shanghai 201800, P. R. China
H. Qi
Hangzhou Institute of Optics and Fine Mechanics
Hangzhou 311421, P. R. China

The ORCID identification number(s) for the author(s) of this article can be found under https://doi.org/10.1002/adom.202300042

DOI: 10.1002/adom.202300042

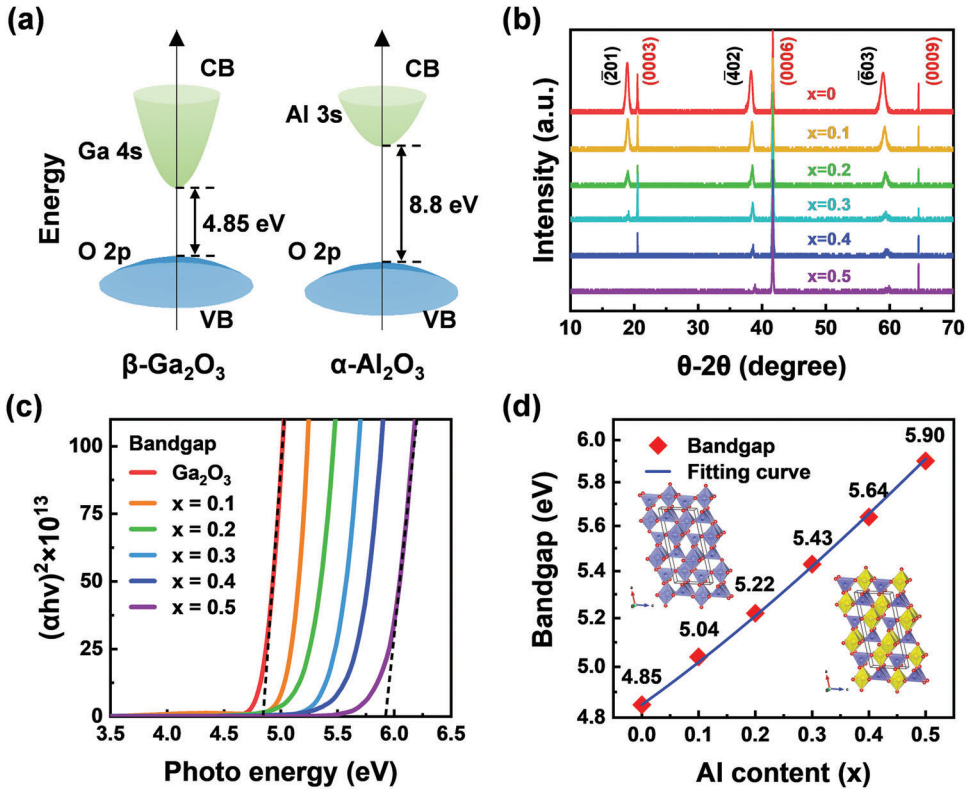

Figure 1. a) Electronic structure of β-Ga_2O_3 and α-Al_2O_3. b) XRD patterns of $(Al_xGa_{1-x})_2O_3$ films with different Al contents (x). c) Tauc plots of $(\alpha h\nu)^2$ versus $h\nu$ for extrapolation of the bandgaps of $(Al_xGa_{1-x})_2O_3$ films. d) Bandgaps of $(Al_xGa_{1-x})_2O_3$ as a function of Al content (x). The insets are the crystal structure of β-Ga_2O_3 and $(Al_{0.5}Ga_{0.5})_2O_3$ used in DFT calculations.

with Ga_2O_3 would modulate the density of states at both edges of the CB and VB, allowing to tune the bandgaps over a wide range and to design of a series of photodetectors sensitive to different wavelengths of the solar-blind UV band. $(Al_xGa_{1-x})_2O_3$ thin films with tunable bandgaps also render it possible to fabricate multispectral solar-blind UV photodetectors.[19,20] Some $(Al_xGa_{1-x})_2O_3$ thin films have been grown using pulsed laser deposition (PLD), metalorganic chemical vapor deposition, and molecular beam epitaxy.[18,21–26] Solar-blind UV photodetectors based on $(Al_xGa_{1-x})_2O_3$ films have also been fabricated.[27–32] However, previous studies have only focused on a few selected Al contents.[28,30,31] To the best of our knowledge, there have not been much systematic study on how the Al contents change the electronic and optical properties of $(Al_xGa_{1-x})_2O_3$. Besides, photodetectors with detection sensitivity to different wavelengths of the solar-blind UV spectrum have not yet been realized.

In this work, we report the tuning of the bandgaps of $(Al_xGa_{1-x})_2O_3$ thin films through varying Al contents, and the achievement of a series of photodetectors with sensitivity to different wavelengths of the entire solar-blind UV regions. We show that the bandgaps of $(Al_xGa_{1-x})_2O_3$ films can be tuned widely from 4.85 to 5.9 eV for $x = 0.5$. Solar-blind ultraviolet photodetectors based on the $(Al_xGa_{1-x})_2O_3$ films show detection cut-off wavelengths varying from 263 to 236 nm, and response peaks varying from 238 to 209 nm. More importantly, the photodetectors exhibit high performance with a high specific detectivity (up to 10^{15} Jones), low dark current (<0.35 nA), large photo-dark current ratio ($\approx 10^5$), UV–vis rejection ratio ($\approx 10^5$), and long-term device stability. We further combined high-resolution X-ray photoemission spectroscopy (XPS) and hybrid density functional theory (DFT) calculations to unravel insights into the evolution of electronic structures of $(Al_xGa_{1-x})_2O_3$ as a function of Al contents.

2. Results and Discussion

2.1. Structural and Optical Properties

Figure 1b shows XRD θ-2θ scans of the $(Al_xGa_{1-x})_2O_3$ films with different Al contents (x) grown on Al_2O_3 (0001) substrates. Bragg peaks corresponding to monoclinic phase Ga_2O_3 ($\bar{2}01$), ($\bar{4}02$), ($\bar{6}03$) crystal planes can be observed, confirming the epitaxial relationship of $(Al_xGa_{1-x})_2O_3$ ($\bar{2}01$)||Al_2O_3 (0001).[33] Figure S1a of the Supporting Information shows zoom-in XRD pattern near the ($\bar{4}02$) reflection. As show in Figure S1b of the Supporting Information, the ($\bar{4}02$) peak shifts to higher 2θ angles with increasing Al contents, indicating a decrease of out-of-plane lattice parameters constants. This could be rationalized from the smaller ionic radius of Al^{3+} (0.53 Å) than Ga^{3+} (0.62 Å), suggesting the success of incorporation of Al in Ga_2O_3 lattice site. However, with the increasing Al contents, the intensity of diffraction peaks of monoclinic phase gradually decreases, indicating degraded crystallinity of the films. Surface morphologies characterized by atomic force microscopy (AFM) are shown in Figure S2a–f of the Supporting Information. All the films show very flat surface morphologies,

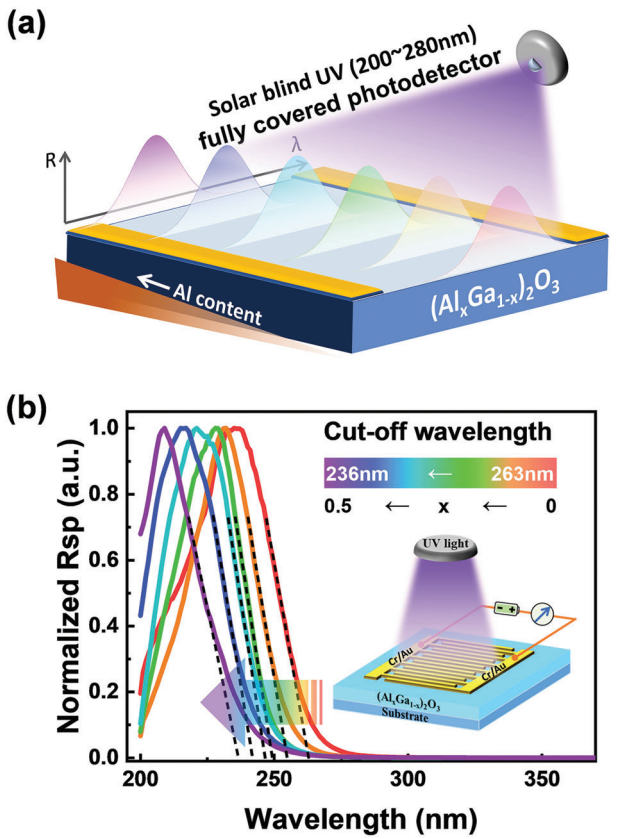

Figure 2. a) Schematics of the $(Al_xGa_{1-x})_2O_3$ bandgap tuning and design of photodetectors sensitive to different wavelengths of solar blind UV bands. b) Normalized photoresponsivity spectra of the $(Al_xGa_{1-x})_2O_3$ based photodetectors, showing the response peaks gradually shift toward shorter wavelengths, the inset shows the MSM device structure.

with small root-mean-square roughness less than 10 nm in 25 μm^2 area. The lower surface roughness will mitigate the effect of the interface state on the contact type of the electrodes of the device.

The optical properties of the $(Al_xGa_{1-x})_2O_3$ films were measured using optical absorption spectroscopy. The optical bandgaps are calculated via Tauc plots of $(\alpha h\nu)^2$ versus $h\nu$, as shown in Figure 1c. The onsets of absorption undergo systematic blue-shift with increasing Al contents, resulting in a systematic increase of bandgaps from 4.85 eV for $x = 0$ to 5.9 eV for $x = 0.5$ (Figure 1d). The variations of bandgaps are in agreement with results predicted by DFT calculation.[16,34] The fitting of the bandgaps conforms to the Vegard's law with a bowing parameter b of 1.08 eV for the $(Al_xGa_{1-x})_2O_3$ alloys. This makes it possible to design solar blind UV photodetectors with tunable detection wavelength.

2.2. Photoelectric Properties of the Solar-Blind Photodetectors

To design photodetectors sensitive to different wavelengths of solar blind UV bands (see **Figure 2**a), we fabricated photodetectors based on metal–semiconductor–metal (MSM) structure (inset in Figure 2b). Figure 2b shows wavelength-dependent photoelectric response of the photodetectors at a bias of 20 V with normalized responsivity (Rsp). With increasing Al contents, the maximum responsivity gradually shifts to shorter wavelengths, e.g., from 238 nm for Ga_2O_3 to 209 nm for $x = 0.5$ devices. The detection cut-off wavelength estimated by linear extrapolation also shifts from 263 to 236 nm. Apparently, the photoresponse bands of the $(Al_xGa_{1-x})_2O_3$ based photodetectors almost cover the entire solar blind UV spectral region. This is consistent with the increase of the optical bandgaps with increase of Al contents observed in Figure 1d.[31]

The typical semilog current–voltage (I–V) characteristics under dark and under light irradiation by the respective response peak wavelengths are shown in **Figure 3**a and Figure S3a (Supporting Information). For Ga_2O_3 devices, the dark current was only ≈300 pA, and a large photocurrent of 3.5 mA was obtained when irradiated. As the Al content increases, the device dark current is largely suppressed. The dark current of the $x = 0.5$ device is as low as 0.9 pA. The response speed of the photodetectors was evaluated by analyzing the rising and decaying edges of the photocurrent in the time-dependent optical response characteristics (I–t), as shown in Figure 3c and Figure S3b (Supporting Information). With the increase of Al content, the rise time is gradually prolonged. On the other hand, the decay time of all devices is very fast and almost indistinguishable. To obtain more information on the dynamic response of the photodetectors, transient photoresponse measurements were performed using a 248 nm pulsed laser as the excitation source to illuminate the devices of $(Al_xGa_{1-x})_2O_3$. The measurement setup is shown in Figure S3d of the Supporting Information. According to the data shown in Figure S3e, the rise time of the devices is generally less than 2 ms, whereas the decay process can be fitted with equation

$$I(t) = I_0 + Ae^{-t/\tau_1} + Be^{-t/\tau_2} \quad (1)$$

where I_0 is the steady-state dark current contribution, A and B are constants, τ_1 and τ_2 are fast and slow decay time constants. Equation (1) simulates the relaxation process of the optical response well and confirms the existence of fast and slow responses. By fitting the decay process, τ_1/τ_2 are derived to be 0.47/13.1 ms for Ga_2O_3 photodetector, 4.2/18.3 ms for $x = 0.1$ photodetector and 12.6/63.7 ms for $x = 0.3$ photodetector. The fast decay can be considered to cause by band-to-band transitions, while the slow response component is caused by the carrier trapping or releasing owing to the existence of defects in Al-alloyed Ga_2O_3 thin films.

We aggregated several key figures-of-merit to evaluate the performance of photodetectors, as shown in Figure 3b and Figure S4 (Supporting Information). Although the photoresponsivity decreases with increasing Al contents, all the photodetectors still maintain high photodark current ratio (PDCR) over 10^4 due to the high response gain derived from the inherent high photosensitivity in the deep UV region. According to the semilog responsivity in Figure S3c of the Supporting Information, the UV–vis rejection ratio (R_{240nm}/R_{400nm}) of the photodetectors is larger than 10^4 or even over 10^5. According to the responsivity, as shown in Figure S4a of the Supporting Information, we can obtain the external quantum efficiency (EQE), which change trend is essentially the same as that of responsivity. For Ga_2O_3, the EQE can be up to 62 600%, indicating that there is considerable gain exists in the device. Furthermore, we also calculated the specific detectivity

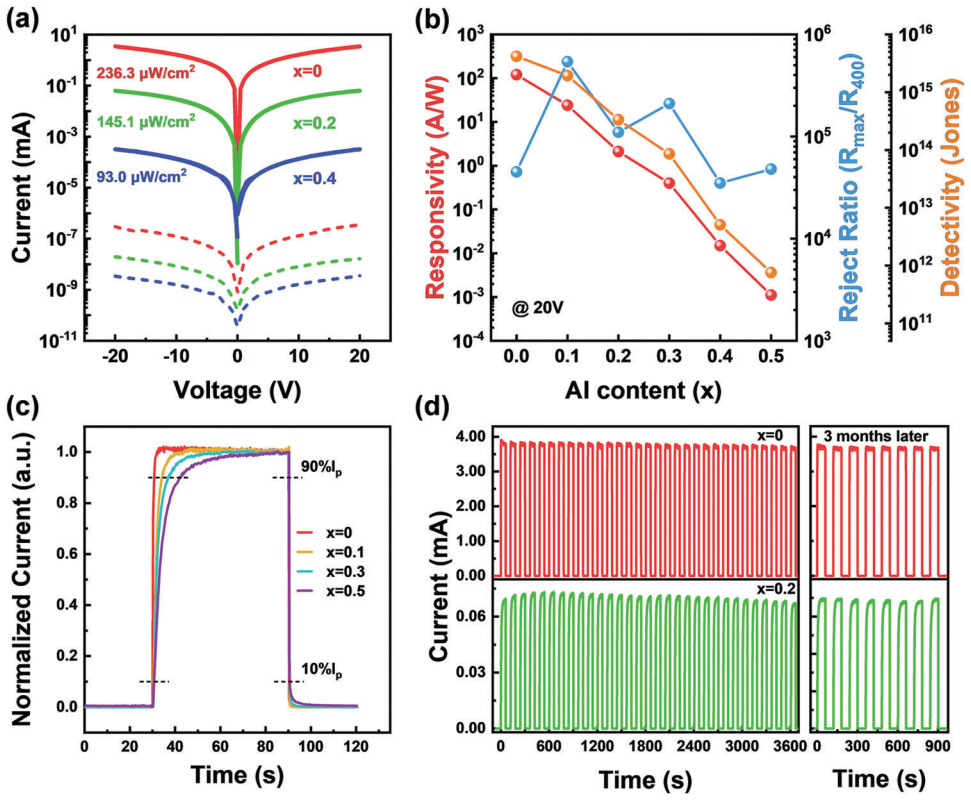

Figure 3. a) *I–V* characteristics of $(Al_xGa_{1-x})_2O_3$ ($x = 0$, $x = 0.2$, $x = 0.4$) photodetectors under dark and light illumination. b) Relationship between responsivity, reject ratio, and detectivity as function of Al contents. c) Normalized time-dependent photoresponse spectra of $(Al_xGa_{1-x})_2O_3$, showing the response speed of photodetector varies with the content of Al-alloying. d) One-hour stability response switch cycle and long-term (3 months) storage reproducibility of the $(Al_xGa_{1-x})_2O_3$ ($x = 0$, $x = 0.2$) photodetectors.

(D^*) and the noise equivalent power (NEP). The NEP is defined as the minimum optical input power required to achieve unity signal-to-noise ratio at 1 Hz frequency, which are employed to assess the ability of sensing the lowest detectable signal according to the following relations

$$D^* = \frac{R_\lambda}{\left(2qI_{\text{dark}}\right)^{1/2}} \tag{2}$$

$$\text{NEP} = \frac{\sqrt{S}}{D^*} \tag{3}$$

where R_λ is the peak responsivity of the corresponding wavelength, q is the electron charge, S is the photosensitive active area, and I_{dark} is the dark current. As shown in Figure S4b of the Supporting Information, the detectivity and NEP for Ga_2O_3 are as high as 4.2×10^{15} Jones and as low as 8.77×10^{-17} W $Hz^{-1/2}$, respectively. However, with increasing Al contents, the corresponding detectivity decreases, but still maintain a value larger than 10^{12} Jones. These values indicate that $(Al_xGa_{1-x})_2O_3$ photodetectors still to remain a high sensitivity to illumination in fully coverage solar-blind spectrum, although this may be caused by the degraded crystalline quality of the grown films with higher Al contents. Nevertheless, photodetectors with higher Al contents still show very high signal-to-noise ratio ($>5 \times 10^4$), PDCR, rejection ratio and low dark current (<0.35 nA) in deep ultraviolet wavelengths. A comparison of the key device parameters of our photodetectors with other reported in literatures is summarized in **Table1**, demonstrating the high performance of our $(Al_xGa_{1-x})_2O_3$ photodetectors with sensitive wavelengths covering the full solar-blind UV spectral region.[14,15,29,30,35–40] Furthermore, we also performed device stability test by continuously switching the device on and off states with 60 s intervals for more than 1 h, as shown in Figures 3d and S5 of the Supporting Information. It can be seen that the devices show consistent performance and there is no obvious functional degradation observed after long-time running. Additionally, there is no performance degradation after storing the devices in dry environments for more than 3 months.

2.3. Electronic Structures of the $(Al_xGa_{1-x})_2O_3$ Films

To reveal insights on the tunable optoelectronic properties of the $(Al_xGa_{1-x})_2O_3$ thin films, we carried out detailed studies on the electronic structure of the $(Al_xGa_{1-x})_2O_3$ using a combination of high-resolution XPS and hybrid DFT calculation. **Figure 4**a shows high-resolution XPS VB spectra of the $(Al_xGa_{1-x})_2O_3$ films. All spectra are referenced to the Fermi level (E_F) as zero. We determined the position of the VB maximum (VBM) of $(Al_xGa_{1-x})_2O_3$ relative to the Fermi level (E_F) by linear extrapolation by analyzing the photoelectron emission spectra of a series

Table 1. Comparisons of performance of solar blind UV photodetectors based on $(Al_xGa_{1-x})_2O_3$ films.

Photodetectors	Rsp [A W^{-1}]	I_{dark} [A]	Wavelength [nm]	$I_{on/off}$	Rej. ratio	Detectivity [Jones]	Voltage [V]	Refs.
UID_Ga_2O_3	120.2	3.5×10^{-10}	238	1.0×10^7	4.5×10^4	4.17×10^{15}	20	This work
$(Al_{0.1}Ga_{0.9})_2O_3$	23.85	6.4×10^{-11}	234	9.9×10^6	5.4×10^5	1.94×10^{15}	20	
$(Al_{0.2}Ga_{0.8})_2O_3$	2.12	1.7×10^{-11}	228	3.7×10^6	1.1×10^5	3.34×10^{14}	20	
$(Al_{0.3}Ga_{0.7})_2O_3$	0.4	9.2×10^{-12}	221	5.3×10^5	2.1×10^5	8.67×10^{13}	20	
$(Al_{0.4}Ga_{0.6})_2O_3$	1.46×10^{-2}	3.5×10^{-12}	217	9.1×10^4	3.5×10^4	5.07×10^{12}	20	
$(Al_{0.5}Ga_{0.5})_2O_3$	1.11×10^{-3}	9.0×10^{-13}	209	1.1×10^4	4.8×10^4	7.60×10^{11}	20	
$(Al_{0.018}Ga_{0.982})_2O_3$	1.38	9.6×10^{-13}	230	$\approx 10^6$	$\approx 10^3$	1.2×10^{13}	5	[35]
$(Al_{0.05}Ga_{0.95})_2O_3$	0.5	8.2×10^{-13}	240	$\approx 7.8 \times 10^4$	$\approx 10^3$	–	5	[29]
$(Al_{0.12}Ga_{0.88})_2O_3$	1.5	–	243	<10	–	–	40	[30]
a-$(Al_{0.12}Ga_{0.88})_2O_3$	0.136	1.2×10^{-9}	230	$\approx 10^3$	≈ 23	2.11×10^{10}	−10	[36]
$(Al_{0.68}Ga_{0.32})_2O_3$	0.086	1.6×10^{-11}	198	$\approx 10^3$	–	–	−10	[37]
ϵ-Ga_2O_3	230	2.3×10^{-11}	254	1.7×10^5	1.2×10^5	1.2×10^{15}	6	[38]
a-Ga_2O_3	733	3.0×10^{-13}	245	3.9×10^7	5×10^3	3.9×10^{16}	5	[39]
$FePSe_3/MoS_2$	3.36×10^4	–	265	–	–	1.51×10^{13}	4	[15]
BiOCl	35.7	1.4×10^{-10}	250	3.06	–	2.2×10^{10}	1	[14]
KNb_3O_8	30	7.1×10^{-15}	254	3.9×10^6	–	5.95×10^{11}	3	[40]

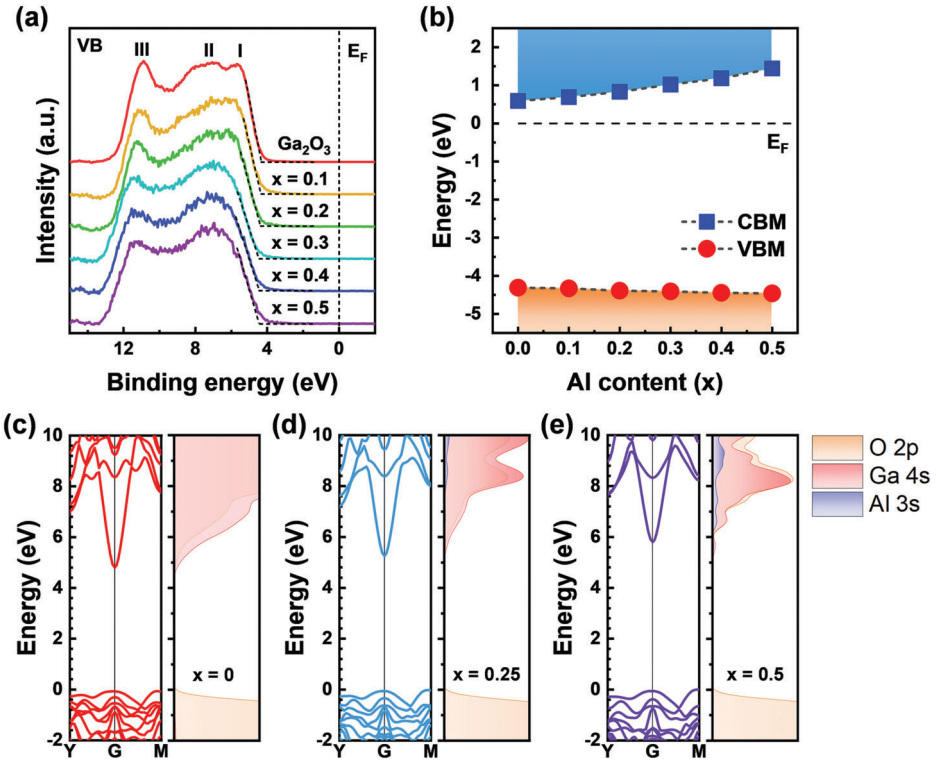

Figure 4. a) XPS valence band (VB) spectra of $(Al_xGa_{1-x})_2O_3$ films. b) The comparison of the band offsets of $(Al_xGa_{1-x})_2O_3$. The position of the CBM is obtained by summing the optical bandgaps extrapolated from absorption spectrum with the XPS VB spectrum. The DFT calculated band structures and the corresponding partial density of states of $(Al_xGa_{1-x})_2O_3$, for c) $x = 0$, d) $x = 0.25$, and e) $x = 0.5$.

of $(Al_xGa_{1-x})_2O_3$. With the increase of Al content, the VBM shift slightly toward higher binding energy, and the density of states of the VB evolves simultaneously. The VBs of Ga_2O_3 show three main features marked as I, II, and III at the binding energy region of 4–13 eV, corresponding to the O $2p^6$ occupied states with minor hybridization with Ga 3d at region I, 4p at region II, and 4s at region III.[41,42] The introduction of Al weakens the degree of hybridization between shallow Ga 3d and O 2p, leading to a gradual decrease in the intensity of region I and the increase of VBM to E_F separation. Furthermore, knowing VBM positions, we

Table 2. The lattice parameters, bandgaps, and electronic effective mass obtained from DFT calculations on the $(Al_xGa_{1-x})_2O_3$ crystal structure with different Al contents.

$(Al_xGa_{1-x})_2O_3$	Lattice parameters				Effective mass [m_e*]	Bandgaps [eV]
x	a [Å]	b [Å]	c [Å]	β [°]		
0	12.200	3.030	5.787	103.85	0.264	4.86
0.25	12.082	2.989	5.747	104.07	0.307	5.28
0.5	11.959	2.946	5.702	104.30	0.360	5.85

can deduce the energy positions of conduction band (CB) by $E_{CB} = E_{VB} + E_g$, where E_g is the corresponding optical bandgap determined from the optical absorption measurements. The corresponding energy diagram is depicted in Figure 4b. For the films with different Al contents, the shift of VBM is relatively small, only about −0.15 eV, while shift of CB is large, e.g., 0.85 eV for $x = 0.5$.

Hybrid DFT calculations were carried out to further examine the evolution of electronic structures of $(Al_xGa_{1-x})_2O_3$ as a function of Al contents. Figure 4c–e and Figure S6 (Supporting Information) shows the calculated band structures and density of states at the edges of VB and CB for $x = 0$, $x = 0.25$, and $x = 0.5$. We note that Al alloying may influence the exciton binding energy. In previous work, Mock et al. reported the band edge exciton binding energy of β-Ga_2O_3 is 120–230 meV.[43] Korlacki et al. found that the exciton binding energy parameters for all β-$(Al_xGa_{1-x})_2O_3$ are kept constant to the values obtained for β-Ga_2O_3.[44] These works suggest that the effect of Al alloying on the exciton binding energy is quite small, and the excitons absorb energy in the alloy very close to the forbidden band energy. We then approximate the fundamental bandgap obtained from the theoretical calculations to the experimentally obtained optical bandgap. **Table 2** shows that the calculated bandgap, lattice parameters, and electronic effective mass are in good agreement with the experimental results, justifying the parameters used for the calculations. With increasing Al contents, the bandgaps are increased to 5.28 and 5.85 eV for $x = 0.25$ and $x = 0.5$, respectively, consistent with the bandgaps measured by optical absorption spectra. More importantly, it can be seen from the band structures that the widening of bandgap of $(Al_xGa_{1-x})_2O_3$ with x mainly results from the upshift of the CB edges. This is because Al alloying introduces empty Al 3s state with a relatively high energy at the CB and the empty Al 3s hybridizes with Ga 4s-derived CB, leading to the upshift of CB edges. However, the VB edges keep the same for all Al contents, because they are mainly composed of occupied O $2p^6$ state with minor hybridization with Ga 3d. Our DFT results also show that the CB edges of $(Al_xGa_{1-x})_2O_3$ are still composed mainly of highly dispersive Ga 4s derived band, leading to a low effective electron mass. This implies that $(Al_xGa_{1-x})_2O_3$ could sustain a high electron mobility for high-performance solar blind UV photodetection application.

3. Conclusions

In summary, we report the tuning of bandgaps of $(Al_xGa_{1-x})_2O_3$ thin films widely from 4.85 to 5.9 eV by systematically varying Al contents, and the achievement of a series of photodetectors with detection wavelengths tunable to entire solar-blind UV regions. The photodetectors also exhibit very high performance with a high specific detectivity (up to 10^{15} Jones), low dark current (< 0.35 nA), large photodark current ratio (≈10^7), UV–vis rejection ratio (>10^5), and long-term device stability. The combined high-resolution XPS and DFT calculations clearly demonstrate that the large variation of the bandgap of $(Al_xGa_{1-x})_2O_3$ mainly results from the upshift of the CB edges induced by the high energy Al 3s state hybridizing with the Ga 4s-derived CB, while the VB edge keeps almost at the same energy. Our results also indicate that the CB edges of $(Al_xGa_{1-x})_2O_3$ with high x are still composed of highly dispersive Ga 4s derived band, giving rise to a low effective electron mass. This implies $(Al_xGa_{1-x})_2O_3$ could sustain a high electron mobility for high-performance photodetector and power electronics applications.

4. Experimental Section

$(Al_xGa_{1-x})_2O_3$ Thin Film Growth: The $(Al_xGa_{1-x})_2O_3$ targets were prepared from Ga_2O_3 and Al_2O_3 polycrystalline powders (99.999%, Alfa Aesar) by grinding, cold pressing, and sintering in air at 1350 °C for 24 h. $(Al_xGa_{1-x})_2O_3$ thin films were epitaxially grown on Al_2O_3 (0001) substrates using PLD using a KrF excimer laser source from respective targets. Laser ablation was performed at a repetition rate of 5 Hz and an energy density of 1.5 J cm^{-2}. The deposited temperature was set at 650 °C with an oxygen background pressure of 10 mTorr. The Al contents in the thin films are the nominal Al mole concentrations in $(Al_xGa_{1-x})_2O_3$ targets used for PLD growth.

Material Characterization: The crystal structure and epitaxial relationship were determined by high-resolution XRD using a PANalytical four-circle diffractometer in θ-2θ scans. Automatic stylus profiler (Bruker Dektak XT-A) was used to estimate the thickness of all the grown films are ≈130 nm. The surface morphology was characterized by AFM (Asylum Research MFP-3D-SA) in tapping mode. Optical absorption measurements were performed at room temperature using a Cary 5000 spectrophotometer in the photon energy range of 1.5–6.2 eV. The electronic structure was performed by high-resolution XPS measurements using a laboratory monochromatic Al $K\alpha_1$ X-ray ($h\nu$ = 1486.6 eV) at normal emission. The high-resolution spectra were collected at a total energy resolution of 0.50 eV. The absolute binding energy scale was calibrated by the Au $4f_{7/2}$ core level at 84.00 ± 0.02 eV.

Device Fabrication and Measurement: Photodetectors were fabricated by comprising 165 pairs of interdigitated electrodes consisting of Cr/Au stacks with thicknesses of 20/50 nm, width of 5 µm, and spacing of 10 µm. The photosensitive active area was calculated as 0.134 cm^2. The spectral response was measured by an automated spectra radiometric measurement system (Zolix DSR-OSX150A) with a 150 W xenon lamp as the excitation source modulated by a mechanical chopper and a monochromator. The incident power density was calibrated by a commercial Si photodiode. Current–voltage (I–V) characteristics were measured using a current source meter (Keithley 2401). Transient photocurrent was measured using a 248 nm pulsed laser (laser pulse width 25 ns) and recorded by an oscilloscope (SIGLENT SDS2102X-E).

DFT Calculations: DFT calculations were performed to further investigate the electronic structure of epitaxial $(Al_xGa_{1-x})_2O_3$ films. The projector augmented wave potentials as implemented in the Vienna Ab initio Simulation Package code was employed with a 450 eV cutoff in the plane-wave expansion and a Γ-centered 6 × 6 × 3 k-point grid. Both PBE and HSE06 were used to relax the structures including pure monoclinic Ga_2O_3 and alloys with different Al concentrations including 25% and 50%. In the monoclinic structure, Al atoms are preferentially occupied octahedral sites.[16] All the structures were considered converged when the forces on all the atoms were less than 0.01 eV $Å^{-1}$. In the HSE06 approach, the mixing parameter α was adjusted to 0.32 to reproduce the experimental bandgap,

which also yields structural parameters that are in better agreement with the experiment.

Supporting Information

Supporting Information is available from the Wiley Online Library or from the author.

Acknowledgements

This work was supported by National Key R&D Program of China (Grant No. 2022YFB3605501), and Shenzhen Science and Technology Program (Grant No. JCYJ20220530143016036).

Conflict of Interest

The authors declare no conflict of interest.

Data Availability Statement

The data that support the findings of this study are available from the corresponding author upon reasonable request.

Keywords

bandgap engineering, gallium oxide, solar-blind ultraviolet photodetectors, thin films, wide bandgap semiconductors

Received: January 7, 2023
Revised: March 3, 2023
Published online:

[1] W. Zheng, R. Lin, J. Ran, Z. Zhang, X. Ji, F. Huang, *ACS Nano* **2018**, *12*, 425.
[2] L. Jia, F. Huang, W. Zheng, *Adv. Opt. Mater.* **2022**, *10*, 2202138.
[3] W. Zheng, L. Jia, F. Huang, *iScience* **2020**, *23*, 101145.
[4] L. Jia, W. Zheng, F. Huang, *Photonix* **2020**, *1*, 22.
[5] M. Razeghi, A. Rogalski, *J. Appl. Phys.* **1996**, *79*, 7433.
[6] M. Razeghi, *Proc. IEEE* **2002**, *90*, 1006.
[7] H. Chen, K. Liu, L. Hu, A. A. Al-Ghamdi, X. Fang, *Mater. Today* **2015**, *18*, 493.
[8] M. Razeghi, *IEEE Photonics J.* **2011**, *3*, 263.
[9] J. Xu, W. Zheng, F. Huang, *J. Mater. Chem. C* **2019**, *7*, 8753.
[10] X. Chen, F. Ren, S. Gu, J. Ye, *Photonics Res.* **2019**, *7*, 381.
[11] W. Chen, X. Xu, J. Zhang, J. Shi, J. Zhang, W. Chen, Q. Cheng, Y. Guo, K. H. L. Zhang, *Adv. Opt. Mater.* **2022**, *10*, 2102138.
[12] J. Shi, J. Zhang, L. Yang, M. Qu, D.-C. Qi, K. H. L. Zhang, *Adv. Mater.* **2021**, *33*, 2006230.
[13] J. Zhang, J. Shi, D.-C. Qi, L. Chen, K. H. L. Zhang, *APL Mater.* **2020**, *8*, 020906.
[14] W. Han, C. Li, S. Yang, P. Luo, F. Wang, X. Feng, K. Liu, K. Pei, Y. Li, H. Li, L. Li, Y. Gao, T. Zhai, *Small* **2020**, *16*, 2000228.
[15] M. Long, Z. Shen, R. Wang, Q. Dong, Z. Liu, X. Hu, J. Hou, Y. Lu, F. Wang, D. Zhao, F. Ding, Y. Tu, T. Han, F. Li, Z. Zhang, X. Hou, S. Wang, L. Shan, *Adv. Funct. Mater.* **2022**, *32*, 2204230.
[16] H. Peelaers, J. B. Varley, J. S. Speck, C. G. Van de Walle, *Appl. Phys. Lett.* **2018**, *112*, 242101.
[17] V. S. Escribano, J. M. G. Amores, E. F. Lopez, M. Panizza, C. Resini, G. Busca, *J. Mater. Sci.* **2005**, *40*, 2013.
[18] F. Zhang, K. Saito, T. Tanaka, M. Nishio, M. Arita, Q. Guo, *Appl. Phys. Lett.* **2014**, *105*, 162107.
[19] M. Gökkavas, S. Butun, H. Yu, T. Tut, B. Butun, E. Ozbay, *Appl. Phys. Lett.* **2006**, *89*, 143503.
[20] J. He, Y. Liu, Z. Li, Z. Ji, G. Yan, C. Zhao, W. Mai, *J. Colloid Interface Sci.* **2022**, *625*, 297.
[21] B. W. Krueger, C. S. Dandeneau, E. M. Nelson, S. T. Dunham, F. S. Ohuchi, M. A. Olmstead, *J. Am. Ceram. Soc.* **2016**, *99*, 2467.
[22] E. Ahmadi, O. S. Koksaldi, X. Zheng, T. Mates, Y. Oshima, U. K. Mishra, J. S. Speck, *Appl. Phys. Express* **2017**, *10*, 071101.
[23] T. Oshima, Y. Kato, N. Kawano, A. Kuramata, S. Yamakoshi, S. Fujita, T. Oishi, M. Kasu, *Appl. Phys. Express* **2017**, *10*, 035701.
[24] R. Tian, M. Pan, Q. Sai, L. Zhang, H. Qi, H. F. Mohamed, *Crystals* **2022**, *12*, 429.
[25] T. Oshima, T. Okuno, N. Arai, Y. Kobayashi, S. Fujita, *Jpn. J. Appl. Phys.* **2009**, *48*, 070202.
[26] A. Bhuiyan, Z. X. Feng, J. M. Johnson, H. L. Huang, J. W. Hwang, H. P. Zhao, *Cryst. Growth Des.* **2020**, *20*, 6722.
[27] L. A. M. Lyle, S. Okur, V. S. N. Chava, M. L. Kelley, R. F. Davis, G. S. Tompa, M. V. S. Chandrashekhar, A. B. Greytak, L. M. Porter, *J. Electron. Mater.* **2020**, *49*, 3490.
[28] H. Y. Lee, J. T. Liu, C. T. Lee, *IEEE Photonics Technol. Lett.* **2018**, *30*, 549.
[29] S.-H. Yuan, S.-L. Ou, C.-C. Wang, S.-Y. Huang, C.-M. Chen, K.-Y. Lin, Y.-A. Chen, D.-S. Wuu, *Jpn. J. Appl. Phys.* **2018**, *57*, 070301.
[30] Q. Feng, X. Li, G. Han, L. Huang, F. Li, W. Tang, J. Zhang, Y. Hao, *Opt. Mater. Express* **2017**, *7*, 1240.
[31] W. Y. Weng, T. J. Hsueh, S. J. Chang, S. C. Hung, G. J. Huang, H. T. Hsueh, Z. D. Huang, C. J. Chiu, *IEEE Sens. J.* **2011**, *11*, 1795.
[32] Z. Li, J. Chen, H. Tang, Z. Zhu, M. Gu, J. Xu, L. Chen, X. Ouyang, B. Liu, *ACS Appl. Electron. Mater.* **2021**, *3*, 4630.
[33] Z. Yang, W. Chen, S. Kuang, Z. Sheng, J. Shi, D. Chen, M. Cui, H. Qi, K. H. L. Zhang, *Cryst. Growth Des.* **2022**, *22*, 7325.
[34] T. Wang, W. Li, C. Ni, A. Janotti, *Phys. Rev. Appl.* **2018**, *10*, 011003.
[35] S.-H. Yuan, C.-C. Wang, S.-Y. Huang, D.-S. Wuu, *IEEE Electron Device Lett.* **2018**, *39*, 220.
[36] S.-B. Liu, S.-J. Chang, S.-P. Chang, C.-H. Chen, *IEEE Photonics J.* **2020**, *12*, 6801908.
[37] Y. Li, D. Zhang, L. Jia, S. Zhu, Y. Zhu, W. Zheng, F. Huang, *Sci. China Mater.* **2021**, *64*, 3027.
[38] Y. Qin, L. Li, X. Zhao, G. S. Tompa, H. Dong, G. Jian, Q. He, P. Tan, X. Hou, Z. Zhang, S. Yu, H. Sun, G. Xu, X. Miao, K. Xue, S. Long, M. Liu, *ACS Photonics* **2020**, *7*, 812.
[39] Y. Qin, L.-H. Li, Z. Yu, F. Wu, D. Dong, W. Guo, Z. Zhang, J.-H. Yuan, K.-H. Xue, X. Miao, S. Long, *Adv. Sci.* **2021**, *8*, 2101106.
[40] Y. Ping, H. Long, H. Liu, C. Chen, N. Zhang, H. Jing, J. Lu, Y. Zhao, Z. Yang, W. Li, F. Ma, X. Fang, Z. Wei, H. Xu, *Adv. Funct. Mater.* **2022**, *32*, 2111673.
[41] J. Y. Zhang, J. Willis, Z. N. Yang, Z. Q. Sheng, L. S. Wang, T. L. Lee, L. Chen, D. O. Scanlon, K. H. L. Zhang, *Phys. Rev. B* **2022**, *106*, 205305.
[42] J. Zhang, J. Willis, Z. Yang, X. Lian, W. Chen, L.-S. Wang, X. Xu, T.-L. Lee, L. Chen, D. O. Scanlon, K. H. L. Zhang, *Cell Rep. Phys. Sci.* **2022**, *3*, 100801.
[43] A. Mock, R. Korlacki, C. Briley, V. Darakchieva, B. Monemar, Y. Kumagai, K. Goto, M. Higashiwaki, M. Schubert, *Phys. Rev. B* **2017**, *96*, 245205.
[44] R. Korlacki, M. Hilfiker, J. Knudtson, M. Stokey, U. Kilic, A. Mauze, Y. Zhang, J. Speck, V. Darakchieva, M. Schubert, *Phys. Rev. Appl.* **2022**, *22*, 064019.